

**Time-dependent population imaging for high-order-harmonic generation in solids**Xi Liu,<sup>1</sup> Xiaosong Zhu,<sup>1,\*</sup> Pengfei Lan,<sup>1,†</sup> Xiaofan Zhang,<sup>1</sup> Dian Wang,<sup>1</sup> Qingbin Zhang,<sup>1</sup> and Peixiang Lu<sup>1,2,‡</sup><sup>1</sup>*School of Physics and Wuhan National Laboratory for Optoelectronics, Huazhong University of Science and Technology, Wuhan 430074, China*<sup>2</sup>*Laboratory of Optical Information Technology, Wuhan Institute of Technology, Wuhan 430205, China*

(Received 17 April 2017; published 22 June 2017)

We propose an intuitive method, called the time-dependent population imaging (TDPI) method, to map the dynamical processes of high-order-harmonic generation (HHG) in solids by solving the time-dependent Schrödinger equation. It is shown that the real-time dynamical characteristics of HHG in solids, such as the instantaneous photon energies of emitted harmonics, can be read directly from the energy-resolved population oscillations of electrons in the TDPI picture. Meanwhile, the short and long trajectories of solid HHG are illustrated clearly from the TDPI picture. By using TDPI, we investigate the effects of the carrier-envelope phase in few-cycle pulses and demonstrate intuitively the HHG dynamics driven by two-color fields. Our results show that TDPI provides a powerful tool to study the ultrafast dynamics in strong fields for various laser-solid configurations and to gain insight into HHG processes in solids.

DOI: [10.1103/PhysRevA.95.063419](https://doi.org/10.1103/PhysRevA.95.063419)**I. INTRODUCTION**

Many interesting strong-field phenomena have been revealed by atoms and molecules interacting with intense laser fields [1–5]. One of the most fascinating phenomena is high-order-harmonic generation (HHG) [6,7]. The HHG from the gas phase has been studied widely over the past several decades [8–10]. Recently, the experimental observation of HHG from bulk solids has attracted extensive attention in the field of attosecond science [11–13]. Apart from having the same advantages as the gas HHG, the solid HHG has the great potential superiority to achieve higher conversion efficiency due to the high density of solid targets [14]. This property makes it a competitive alternative for obtaining the tabletop extreme ultraviolet (XUV) light source [15,16]. In addition, solid HHG provides a useful tool to probe the energy-band structures of crystals [17] and even to image the orbitals of solids [18]. For example, Vampa *et al.* [19] reconstructed the energy bands of ZnO crystal based on the HHG method. The solid HHG has opened up a new frontier to study the attosecond electron dynamics in condensed matter [20].

For the solid HHG, the particular characteristics distinguishing it from gas HHG essentially stem from the periodicity and high density of the crystal. At present, the driving wavelengths for solids are centered in the midinfrared (MIR) [11,21] and terahertz [22,23] regions. With such long wavelengths, the laser intensity can be moderate and thus lower than the damage threshold. The harmonic spectra from solids exhibit evident multiple plateaus [24,25] and extend well beyond the atomic limit. The cutoff energy of the solid HHG shows a linear dependence on field strength [11,12], unlike the quadratic dependence relation in gas HHG. The ellipticity dependence of solid HHG is complicated. The experimental result shows that the ellipticity dependence of HHG from ZnO crystal is much weaker than that of gas HHG [11], whereas

the HHG from rare-gas solids shows an ellipticity dependence as strong as that from gaseous atoms [18].

The mechanism of HHG in solids has been a topic of intense debate [26–28]. Most works consider that the HHG in solids originates from two distinct contributions: an intraband current in the individual bands and an interband current involving the transitions between the valence and conduction bands. Theoretical analyses show that the interband current dominates the HHG for MIR driver pulses [29–31]. Vampa *et al.* [32,33] proposed an electron-hole recollision model to describe the mechanism, where electrons in conduction bands recombine with associated holes in the valence band. Meanwhile, Wu *et al.* [24,25] suggested that the primary plateau originates from the transitions from the first conduction band to the valence band and the latter plateaus are due to transitions from higher-lying conduction bands. However, when driving wavelengths are extended toward the terahertz regime, the intraband current caused by laser-driven Bloch oscillations becomes dominant for the HHG processes [30,34–36]. Currently, although some theoretical models can explain the solid HHG very well, an intuitive method to describe the picture of HHG in solids is still an urgent need.

In this work, we propose an intuitive picture, named time-dependent population imaging (TDPI) picture, to reveal the HHG process in solids. In the TDPI picture, the real-time dynamics of HHG are mapped via the population oscillations of electrons at different energy bands. The features of HHG can be directly decoded from TDPI pictures. For example, the photon energies of real-time harmonic emissions can be read from the instantaneous energy differences between the oscillating electrons in different bands. In particular, the cutoff energies are obtained according to the maximum energy differences shown in TDPI pictures. The short and long trajectories of solid HHG can be distinguished clearly in the TDPI picture. The effects of the carrier-envelope phase (CEP) in few-cycle pulses and HHG processes in two-color fields are also demonstrated by using the TDPI pictures. The TDPI approach can be used to visualize the solid HHG dynamics and advance our understanding of strong-field and attosecond physics in solids.

\*zhuxiaosong@hust.edu.cn

†pengfeilan@mail.hust.edu.cn

‡lupeixiang@mail.hust.edu.cn

This paper is organized as follows. In Sec. II, we describe the theoretical model and numerical method in our simulations. In Sec. III, we introduce the TDPI picture and predict the starting and cutoff energies of solid HHG with the TDPI pictures. In Sec. IV, the concepts of short and long trajectories for solid HHG are established based on TDPI pictures. In Sec. V, the TDPI picture is used to explain the CEP effect in solid HHG. In Sec. VI, TDPI picture is used to reveal the HHG processes driven by two-color fields, and the effect of the relative phase between the two components on the HHG dynamics is discussed. We summarize our work in Sec. VII.

## II. THEORETICAL MODEL

In our simulation, we describe the laser-crystal interaction with a one-dimensional single-active electron system. The laser field is polarized along the crystal axis. Since the wavelengths we are interested in are much larger than the lattice constant, dipole approximation is valid and has been employed in our calculation. In the length gauge, the time-dependent Hamiltonian reads (atomic units are used throughout this paper unless otherwise stated)

$$\hat{H}(t) = \hat{H}_0 + xF(t), \quad (1)$$

where  $\hat{H}_0$  is the field-free Hamiltonian and  $F(x)$  is the electric field of the driving laser.  $\hat{H}_0$  is written as  $\hat{H}_0 = \hat{p}^2/2 + V(x)$ , where  $\hat{p}$  is the momentum operator and  $V(x)$  is the periodic lattice potential. Herein, we use the Mathieu-type potential  $V(x) = -V_0[1 + \cos(2\pi x/a_0)]$ , with  $V_0 = 0.37$  a.u. and lattice constant  $a_0 = 8$  a.u. The Mathieu-type potential [37] is a typical model potential and has been used extensively in the optical lattice research area [38,39] and recent solid HHG studies [24,25,31,40,41]. We perform all calculations in the coordination space with the region  $[-240, 240]$  a.u. (60 lattice periods).

The energy-band structure of a crystal is obtained by solving the eigenvalue equation of the field-free Hamiltonian  $\hat{H}_0$ ,

$$\hat{H}_0\phi_n(x) = E_n\phi_n(x), \quad (2)$$

where  $n$  is the eigenstate number and  $\phi_n(x)$  is the corresponding eigenstate wave function. We numerically solve Eq. (2) by diagonalizing  $\hat{H}_0$  on a coordinate grid. Specifically, the  $\hat{H}_0$  operator is represented by an  $N \times N$  square matrix  $\mathbf{H}$ , where  $N$  is the number of grid points. The nonzero elements of the matrix  $\mathbf{H}$  are given by

$$\begin{aligned} \mathbf{H}_{i,i} &= \frac{1}{(\Delta x)^2} + V_i, \\ \mathbf{H}_{i,i+1} &= -\frac{1}{2(\Delta x)^2}, \\ \mathbf{H}_{i+1,i} &= \mathbf{H}_{i,i+1}, \end{aligned} \quad (3)$$

where  $\Delta x$  is the grid spacing and  $V_i$  is the  $i$ th element of the one-dimensional grid of  $V$ . The eigenenergy  $E_n$  and eigenstate  $\phi_n(x)$  are obtained by solving the eigenvalues and eigenvector of matrix  $\mathbf{H}$ .

Figure 1(a) shows the band structures calculated with the diagonalization scheme, where the band groups can be clearly distinguished. As illustrated in Fig. 1(a), the five bands are denoted as VB0, VB, CB1, CB2, and CB3, respectively. The

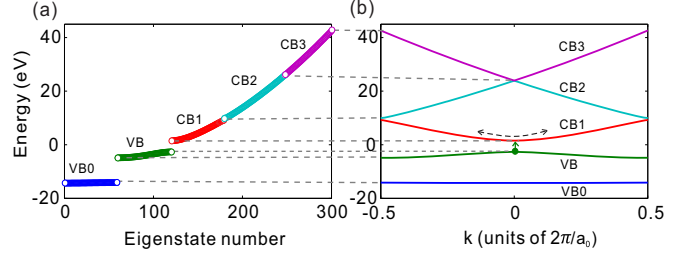


FIG. 1. The band structures calculated by (a) the diagonalization scheme in coordinate space and (b) Bloch-state expansion in reciprocal space. Five bands are shown.

state numbers corresponding to the five bands are 1–59, 60–120, 61–180, 181–240, and 241–300, respectively. In order to verify the accuracy of the resulting bands, we calculate the band structure by using the Bloch-state basis [25]. The obtained band structure is shown in Fig. 1(b). One can see that the features of the bands (such as the number of bands and the energy range of each band) obtained by the two methods are in good agreement, which confirms the accuracy of our resulting ground states and field-free bands.

When solids are irradiated by a laser pulse, electrons in the valence bands have opportunities to tunnel into conduction bands. The tunneling probability exponentially decays with the increase in band gap. Considering the laser parameters used in current works, only a small proportion of electrons near  $k = 0$  in the valence band (VB) can tunnel into conduction bands [as indicated by the solid green arrow in Fig. 1(b)]. We have confirmed that the HHG is contributed mainly by the initial distribution of population near  $k = 0$  by calculating the harmonic spectra with the initial states with different  $k$  in VB. Therefore, we choose the eigenstate with  $k = 0$  in VB as the initially populated state. The same treatment has been adopted in previous works [24,31,40,41]. Since the lowest band, VB0, is very flat and deeply bound, it plays a negligible role in the HHG dynamics. The time-dependent wave function  $\psi(t)$  is obtained by solving the time-dependent Schrödinger equation (TDSE) using the split-operator technique [42]. The time step is 0.03 a.u. An absorbing boundary is adopted to overcome the unphysical reflections at the edges of the grid. In our calculation, the width of the absorbing boundary is adopted as 40 a.u. The wavelengths of the driving laser pulses are restricted in the MIR region. We adopt a sine-squared envelope [43] for all laser pulses in this work.

The harmonic spectrum is obtained by calculating the Fourier transform of the laser-induced current:

$$H(\omega) = \frac{2}{3\pi c^3} \left| \int j(t) e^{i\omega t} dt \right|^2, \quad (4)$$

where  $c$  is the speed of light. The laser-induced current  $j(t)$  is given by [31]

$$j(t) = -\langle \psi(t) | \hat{p} | \psi(t) \rangle. \quad (5)$$

In order to improve the signal-to-noise ratio, we multiply  $j(t)$  by a Hanning window [25] before the Fourier transformation since the laser intensities adopted in the present work are relatively low.

To obtain the TDPI picture for the solid HHG, the instantaneous population of electrons on each eigenstate should be calculated during the TDSE propagation. The instantaneous population  $|C_n(t)|^2$  on eigenstate  $\phi_n$  is obtained by calculating the modulus square of the time-dependent projection of  $\psi(t)$  on  $\phi_n$  as

$$|C_n(t)|^2 = |\langle \phi_n | \psi(t) \rangle|^2. \quad (6)$$

Since  $\phi_n$  corresponds to the various eigenenergies  $E_n$ ,  $|C_n(t)|^2$  can be understood as the time-dependent probability of electrons occupying the energy level  $E_n$ . Then the TDPI picture is obtained by plotting  $|C_n(t)|^2$  as a function of time  $t$  and eigenenergy  $E_n$ . The time- and energy-resolved population evolution describes the electron dynamics in solid HHG. Apparently, the TDPI method is not limited to the one-dimensional structure and can be extended to the more complex solid targets, such as graphene [44,45].

### III. STARTING AND CUTOFF ENERGIES OF PLATEAUS

Figure 2(a) shows the calculated TDPI picture for an HHG process driven by a laser pulse with wavelength  $\lambda = 3.20 \mu\text{m}$  and intensity  $I = 8.09 \times 10^{11} \text{ W/cm}^2$ . The total duration of the adopted laser pulse is eight optical cycles. The optical cycle of the laser field is denoted as  $T_0$ . Several features can be found from the TDPI picture shown in Fig. 2(a). One can see clear energy-resolved population oscillations of electrons in the respective bands. These population oscillations correspond to the laser-driving Bloch oscillations of electrons in reciprocal space, where the electrons are driven forth and back periodically by the external laser field [as indicated by the dashed black arrows in Fig. 1(b)]. The strong oscillations shown in the TDPI picture indicate that the solid HHG is a highly delocalized process, unlike the gas HHG process, where electrons are mainly localized in the ground state. The profiles of population oscillations shown in VB and CB1 are clear and bright. However, the profiles in CB2 and CB3 become blurry. This is because it is more difficult to populate the laser-driven electrons into higher conduction bands, and therefore, the corresponding electron populations are about three orders of magnitude lower than that in CB1. Some striplike structures appear at the bottom of CB2, which are caused by the spread of the wave packet. Considering that the population oscillations are blurred by the striplike structures, we indicate the oscillation peaks using solid white curves in the blurred region.

The obtained harmonic spectrum is shown in Fig. 2(b). One can clearly see a characteristic two-plateau structure, as described in Refs. [25,31], where each plateau has a start and a cutoff. The harmonic spectrum extends over many orders of magnitude in yield. This is because the intensity of the second plateau is more than five orders of magnitude lower than that of the first plateau, as pointed out by Wu *et al.* [25]. The second plateau has been observed in a recent experiment [18]. As in previous studies [25,33,46], the harmonic spectrum exhibits clear odd harmonics in the low-energy region and noisy continuumlike structures in both the first and second plateaus. The absence of clear harmonics in plateaus can be ascribed to several reasons, such as the infinitely long dephasing time [33], elastic or inelastic scattering processes [28], etc. As discussed in Refs. [24,25], the HHG process can be understood with the

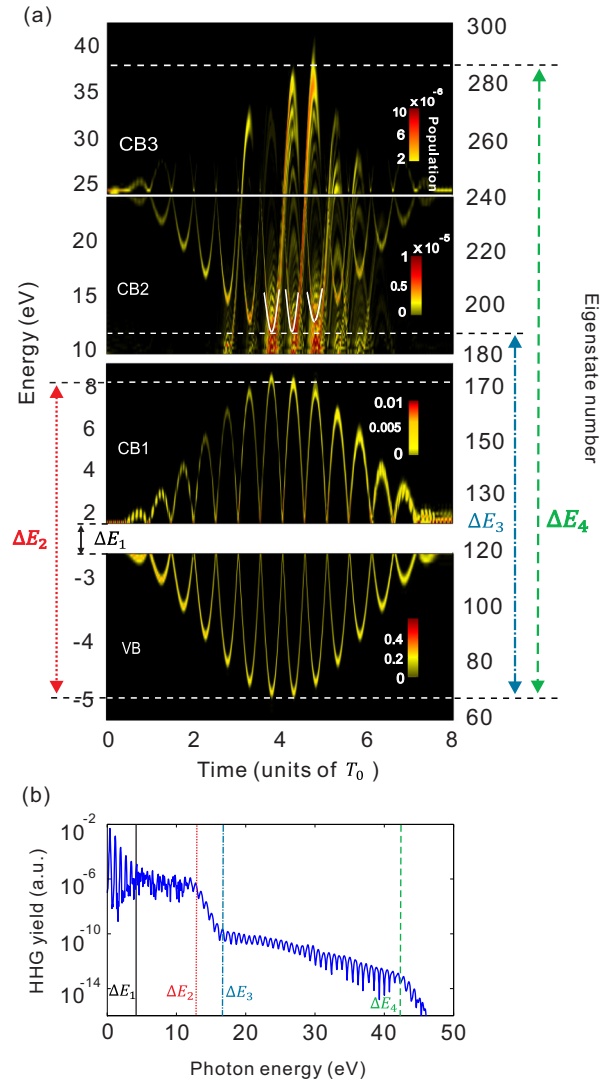


FIG. 2. The (a) TDPI picture and (b) harmonic spectra obtained with laser wavelength  $\lambda = 3.20 \mu\text{m}$  and laser intensity  $I = 8.09 \times 10^{11} \text{ W/cm}^2$ . The total pulse duration is eight cycles. In the TDPI picture, the horizontal white dashed lines indicate the maximum and minimum instantaneous energies of the oscillating electrons. The oscillation peaks in CB2 are indicated by the white solid curves for much clearer observations.  $\Delta E_1$  and  $\Delta E_3$  represent the minimum energy differences read from the TDPI picture.  $\Delta E_2$  and  $\Delta E_4$  represent the maximum energy differences read from the TDPI picture.

TDPI picture as follows. For the first plateau, the oscillating electron shown in the TDPI picture undergoes a transition from CB1 to VB, accompanied by the emission of a harmonic photon. The real-time photon energy of the emitted harmonic is equal to the instantaneous energy difference of oscillating electrons in corresponding bands. Similarly, the second plateau is contributed by a transition of oscillating electrons from CB2 and CB3 to VB. In the discussion, CB2 and CB3 are considered as a whole because CB2 and CB3 are very close and strongly coupled to each other.

Based on the above viewpoint, the starting and cutoff energies of both the first and second plateaus can be

predicted exactly from TDPI pictures. In the following discussion, the instantaneous energies corresponding to the population oscillation in VB, CB1, CB2, and CB3 shown with TDPI pictures are denoted as  $\mathcal{E}_{\text{VB}}(t)$ ,  $\mathcal{E}_{\text{CB1}}(t)$ ,  $\mathcal{E}_{\text{CB2}}(t)$ , and  $\mathcal{E}_{\text{CB3}}(t)$ , respectively. When electrons undergo the transitions from CB1 to VB, the minimum energy difference  $\Delta E_1$  and maximum energy difference  $\Delta E_2$  are obtained, respectively, by

$$\Delta E_1 = \min[\mathcal{E}_{\text{CB1}}(t) - \mathcal{E}_{\text{VB}}(t)], \quad (7)$$

$$\Delta E_2 = \max[\mathcal{E}_{\text{CB1}}(t) - \mathcal{E}_{\text{VB}}(t)]. \quad (8)$$

As shown in Fig. 2(a),  $\Delta E_1$  and  $\Delta E_2$  can be easily read from the TDPI picture.  $\Delta E_1$  is equal to the band gap between VB and CB1.  $\Delta E_2$  is the energy difference between the highest (or deepest) peaks of population oscillations in VB and CB1, as indicated by the dashed white lines. Considering that the first plateau originates from the transitions from CB1 to VB,  $\Delta E_1$  and  $\Delta E_2$  should correspond to the starting and cutoff energies of the first plateau, respectively. As shown in Fig. 2(b),  $\Delta E_1$  and  $\Delta E_2$  are indicated by the solid black and dotted red lines in the harmonic spectrum, respectively. One can see that the positions of  $\Delta E_1$  and  $\Delta E_2$  agree very well with the start and cutoff of the first plateau, respectively. Similarly, for the transitions from CB2 and CB3 to VB, the minimum energy difference  $\Delta E_3$  and maximum energy difference  $\Delta E_4$  are given by

$$\Delta E_3 = \min[\mathcal{E}_{\text{CB2}}(t) - \mathcal{E}_{\text{VB}}(t)], \quad (9)$$

$$\Delta E_4 = \max[\mathcal{E}_{\text{CB3}}(t) - \mathcal{E}_{\text{VB}}(t)]. \quad (10)$$

$\Delta E_3$  and  $\Delta E_4$  can also be easily found in Fig. 2(a). The second plateau is caused by the transitions from CB3 and CB2 to VB. Therefore, as shown in Fig. 2(b) by the dot-dashed cyan and dashed green lines, respectively,  $\Delta E_3$  and  $\Delta E_4$  match the starting and cutoff energies of the second plateau accurately. The correspondence between the starting (cutoff) energy of the plateau and the minimum (maximum) energy difference in the TDPI picture has been verified by our other simulations with different laser parameters. In addition, the low harmonic intensity of the second plateau can be interpreted by the minor numbers of populations in CB2 and CB3. Specifically, there are fewer electrons contributing to the transitions from CB2 and CB3 to VB than those from CB1 to VB.

In previous discussions, the population oscillations of electrons have been confined within the respective bands. Then, a question arises. Is the cutoff energy of a plateau confined by the energy range of the involved bands (including band gaps)? For example, we denote the total span between the bottom of VB and top of CB1 as  $E_{\text{VC1}}$ , which is indicated in Fig. 3(a) by a purple arrow. Will the cutoff energy of the first plateau not extend  $E_{\text{VC1}}$ ? In order to answer that question, we calculate the TDPI picture and harmonic spectrum with a laser pulse of wavelength  $\lambda = 4.00 \mu\text{m}$  and intensity  $I = 1.20 \times 10^{12} \text{ W/cm}^2$ . Such a longer wavelength and higher intensity can populate the electrons to higher levels. In the following discussion, we will focus on only the first plateau since the second plateau is much weaker.

The obtained TDPI picture and harmonic spectrum are shown in Figs. 3(a) and 3(b), respectively. From Fig. 3(a), one can see that, when the oscillating electrons in CB1 reach

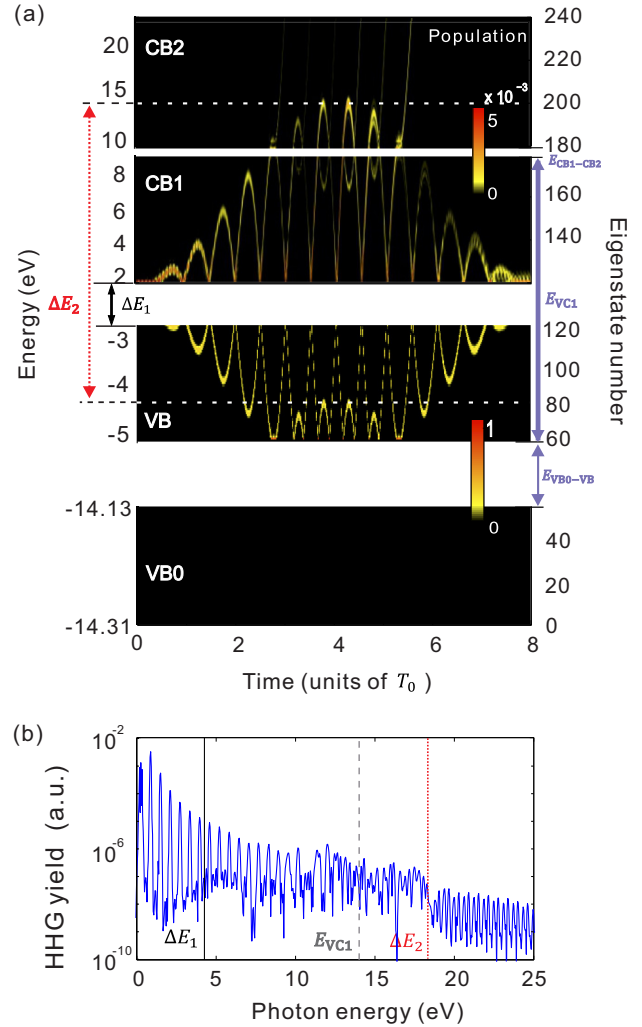


FIG. 3. The (a) TDPI picture and (b) harmonic spectrum obtained with laser wavelength  $\lambda = 4.00 \mu\text{m}$  and laser intensity  $I = 1.20 \times 10^{12} \text{ W/cm}^2$ . The gray dashed line indicates the total span of VB and CB1  $E_{\text{VC1}}$ .

the top of the band (the boundary of the first Brillouin zone in reciprocal space), the electrons can tunnel through the band gap into CB2. The tunneling electrons in CB2 will continue oscillating in the laser field. In order to focus on the population oscillations of electrons tunneling from CB1, we adopt the same color scale for CB1 and CB2. The band gap between CB1 and CB2 is very narrow ( $E_{\text{CB1-CB2}} = 0.84 \text{ eV}$ ). Therefore, oscillating electrons in CB1 can tunnel into CB2 easily. In contrast, when oscillating electrons in VB reach the bottom of the band, the electrons can hardly tunnel into VB0 since the band gap between VB0 and VB is quite broad ( $E_{\text{VB0-VB}} = 9.25 \text{ eV}$ ). From the TDPI picture shown in Fig. 3(a), it is concluded that, because the oscillating electrons can tunnel into higher bands with a high probability, the possible cutoff energy is not limited by the energy range of the involved bands. In Fig. 3(a), the maximum energy difference  $\Delta E_2$  for the first plateau is indicated by the dotted red arrow, which spans from the highest oscillation peak in CB2 to that in VB. As shown in Fig. 3(b),  $\Delta E_2$  is in good agreement with the cutoff energy of the first plateau in the harmonic spectrum. As

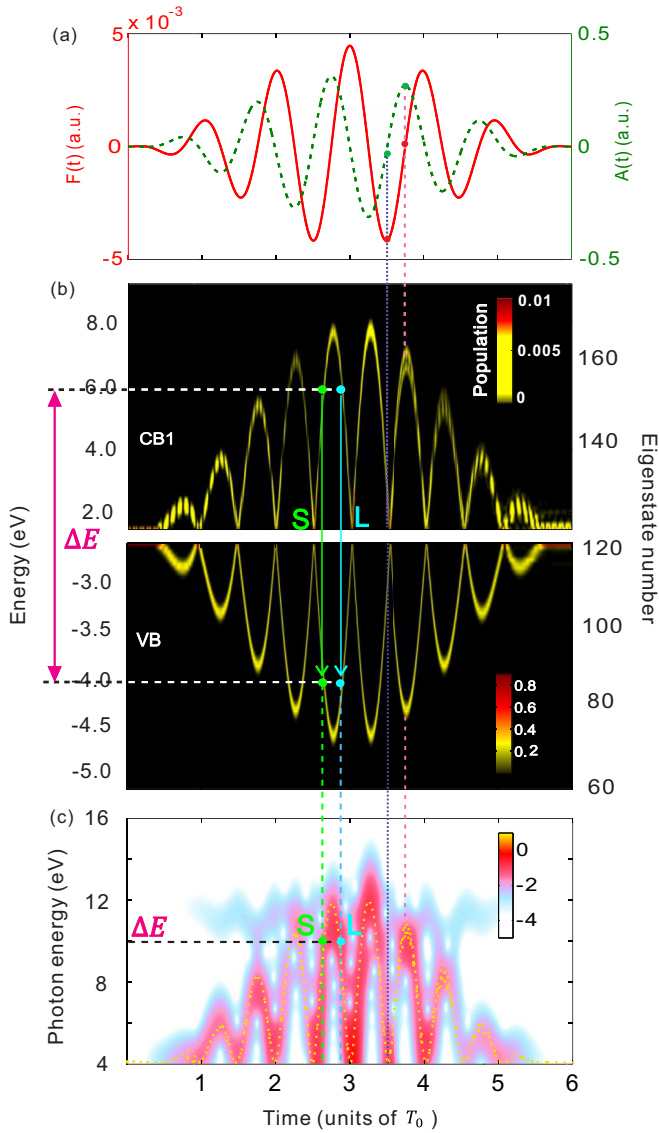


FIG. 4. (a) The electric field and vector potential of the laser pulse with laser wavelength  $\lambda = 3.20 \mu\text{m}$  and laser intensity  $I = 7.00 \times 10^{11} \text{ W/cm}^2$ . The total duration is six optical cycles. (b) The TDPI picture obtained with the field shown in (a). (c) The time-frequency spectrum with a logarithmic color scale. The dotted yellow curve is the instantaneous energy difference of oscillating electrons in CB1 and VB obtained from the TDPI picture. In (b) and (c), S and L denote the short and long trajectories.

expected,  $\Delta E_2$  is larger than  $E_{\text{VC1}}$ , where  $E_{\text{VC1}}$  is indicated by the dashed gray line.

#### IV. EMISSION TIME AND TRAJECTORY ANALYSIS

In this section, the emission times of high harmonics in solids will be discussed with TDPI pictures. Figure 4(b) shows the calculated TDPI picture for the HHG process driven by a  $3.20\text{-}\mu\text{m}$  laser pulse with an intensity of  $7.00 \times 10^{11} \text{ W/cm}^2$ . The pulse duration is six optical cycles. The electric field and vector potential of the laser pulse are plotted in Fig. 4(a). In order to obtain the emission times of harmonics, we calculate

the time-frequency (TF) spectrum using the Gabor transform [47] of the time-dependent current. The resulting TF spectrum is shown in Fig. 4(c). One can see that the harmonic emissions occur four times per optical cycle. For each half cycle, the emissions correspond to a pair of short and long branches (labeled S and L, respectively). From Figs. 4(a)–4(c), it is found that the evolution of the time-dependent population in the TDPI picture agrees well with the profile of the TF spectrum. The peaks of population oscillations in the TDPI picture and HHG radiations in the TF spectrum both correspond to the zero points of laser fields and peaks of vector potentials, as indicated by the dashed pink lines. On the contrary, the minima of population oscillations and HHG radiations both correspond to the peaks of laser fields and zero points of vector potentials, as indicated by dotted purple lines. Furthermore, we calculate the instantaneous energy differences of oscillating electrons in CB1 and VB, i.e.,  $\mathcal{E}_{\text{C1-V}}(t)$ .  $\mathcal{E}_{\text{C1-V}}(t)$  is obtained from the TDPI picture shown in Fig. 4(b) as

$$\mathcal{E}_{\text{C1-V}}(t) = \mathcal{E}_{\text{CB1}}(t) - \mathcal{E}_{\text{VB}}(t). \quad (11)$$

We plot  $\mathcal{E}_{\text{C1-V}}(t)$  as the yellow dotted curve in Fig. 4(c). One can see that  $\mathcal{E}_{\text{C1-V}}(t)$  is consistent with the harmonic signals shown in the TF spectrum very well. In the studies of gas HHG, the TF spectrum is one of the most important and frequently used tools to analyze the HHG dynamics. Likewise, the TDPI picture can also be a useful tool for a solid HHG like the TF spectrum.

In gas HHG, a semiclassical three-step model builds up an intuitive picture to describe the HHG process [8]. In this picture, the short and long trajectories are distinguished according to the duration of the tunneling electrons traveling in the continuum [9]. As shown in Fig. 4(c), the “short” and “long” trajectories still exist in solid HHG and can be seen from the TF spectrum. Based on the TDPI method, the concepts of short and long trajectories for solid HHG can be established according to the short and long branches of the population oscillations within the same half cycle. For example, for the harmonic with photon energy  $\Delta E = 9.96$  eV, the emission occurs twice per half cycle, as shown in Fig. 4(b). As denoted by the solid green (left) arrow, the transition from the short branch occurs at time  $t_S = 2.63 T_0$ . Then the electrons oscillate to higher energies and return back to the same energy level at time  $t_L = 2.87 T_0$ , and subsequently, a harmonic photon with the same energy  $\Delta E = 9.96$  eV is emitted via the transition from the long branch, as denoted by the solid cyan (right) arrow. The emission time  $t_S$  is earlier than  $t_L$ . Therefore, the emission pathways indicated by the green and cyan arrows can be called short and long trajectories, respectively. The short and long trajectories read from TDPI pictures are consistent with those shown in the TF spectrum. As shown in Fig. 4(c), for the harmonic with photon energy  $\Delta E = 9.96$  eV,  $t_S$  and  $t_L$  are in good agreement with those read from the short and long branches of the TF spectrum, respectively. Moreover, as in the gas HHG, the short trajectory of the solid HHG is positively chirped, whereas the long trajectory is negatively chirped. In reciprocal space, the short and long trajectories appear essentially because the electrons are driven forth and back during the Bloch oscillation and will pass the same point (with specific  $k$ ) twice in one half cycle.

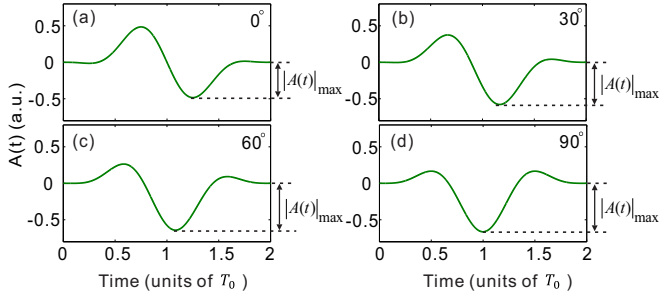


FIG. 5. Vector potentials of laser pulses with different CEPs. (a)  $\phi = 0^\circ$ . (b)  $\phi = 30^\circ$ . (c)  $\phi = 60^\circ$ . (d)  $\phi = 90^\circ$ . The laser wavelength is  $\lambda = 3.60 \mu\text{m}$ , and the laser intensity is  $I = 1.40 \times 10^{12} \text{ W/cm}^2$ . The total duration is two optical cycles.  $|A(t)|_{\text{max}}$  represents the maximum value of the module of vector potentials  $A(t)$ .

### V. CARRIER-ENVELOPE PHASE EFFECT

For a few-cycle laser pulse, the CEP will dramatically affect the temporal shape of the electric field. Some physical processes induced by the few-cycle laser field will rely on the variation of CEP. For example, the cutoff energy of the gas HHG sensitively depends on the CEP of the driving field [48,49]. The CEP effect has been discussed widely for photoionization [50–52] and gas HHG [53,54].

In this section, we will analyze the CEP effect for solid HHG by using the TDPI picture. The adopted laser wavelength is  $\lambda = 3.60 \mu\text{m}$  and laser intensity is  $I = 1.40 \times 10^{12} \text{ W/cm}^2$ . The total duration of the laser pulse is two optical cycles. Figures 5(a)–5(d) show the vector potentials of the laser pulses with CEP  $\phi = 0^\circ, 30^\circ, 60^\circ$ , and  $90^\circ$  respectively. The maximum of the module of vector potentials  $|A(t)|_{\text{max}}$  is indicated with the vertical arrows. In the following discussion, we will focus on the first cutoff. The cutoff energy is denoted as  $\eta_{\text{cutoff}}$ .

High-order-harmonic spectra for  $\phi = 0^\circ, 30^\circ, 60^\circ$ , and  $90^\circ$  are shown in Fig. 6(a). One can clearly see that the cutoff energy  $\eta_{\text{cutoff}}$  is very sensitive to the CEP. Specifically, as indicated by the dashed purple curve,  $\eta_{\text{cutoff}}$  increases monotonously when  $\phi$  varies from  $0^\circ$  to  $90^\circ$ . In order to further discuss the relation between  $\eta_{\text{cutoff}}$  and  $\phi$ , we calculate the cutoff energy  $\eta_{\text{cutoff}}$  as a function of  $\phi$  from  $0^\circ$  to  $360^\circ$  in steps of  $15^\circ$ . The obtained result is shown in the Fig. 6(b) as the solid blue curve. Here  $\eta_{\text{cutoff}}$  is read from  $\Delta E_2$  shown in the corresponding TDPI picture because  $\eta_{\text{cutoff}}$  is equal to the maximum energy difference  $\Delta E_2$ , as discussed in Sec. III. One can see that  $\eta_{\text{cutoff}}$  exhibits the tendency of monotonous increasing in the region of  $0^\circ$ – $90^\circ$ , which corresponds to the results shown in Fig. 6(a). Our further studies show that  $\eta_{\text{cutoff}}$  has a close relation to  $|A(t)|_{\text{max}}$ .  $|A(t)|_{\text{max}}$  as a function of  $\phi$  is shown as the dashed green curve in Fig. 6(b). It is found that the  $|A(t)|_{\text{max}}$  and  $\eta_{\text{cutoff}}$  curves are nearly in complete agreement with each other. This indicates that  $\eta_{\text{cutoff}}$  is determined by the corresponding  $|A(t)|_{\text{max}}$ . Considering that the  $\eta_{\text{cutoff}}$  and  $|A(t)|_{\text{max}}$  curves are plotted with different linear vertical axes, it can be speculated that  $\eta_{\text{cutoff}}$  depends linearly on  $|A(t)|_{\text{max}}$ , i.e.,

$$\eta_{\text{cutoff}} \propto |A(t)|_{\text{max}}. \quad (12)$$

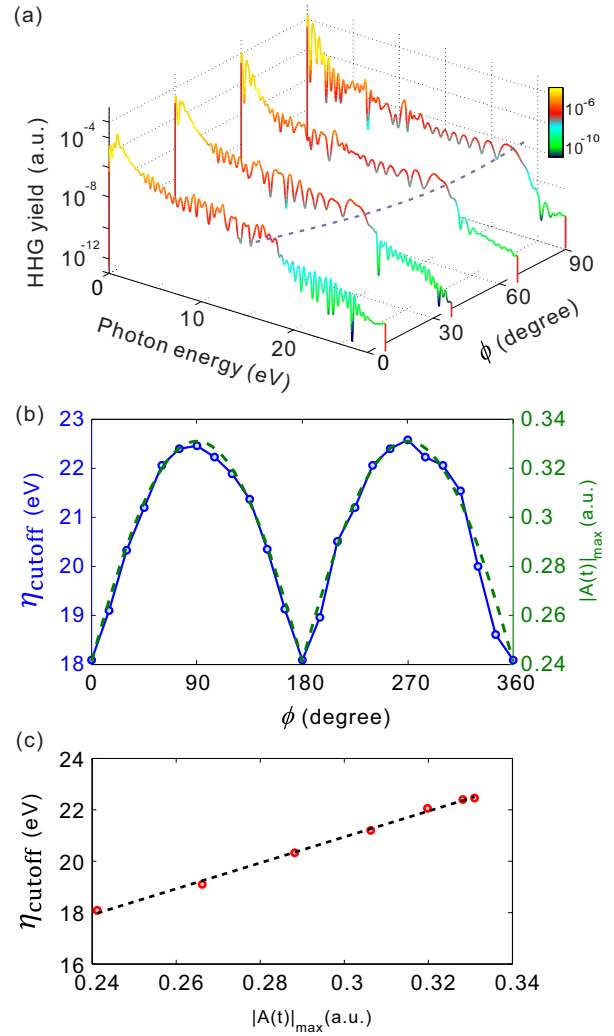


FIG. 6. (a) High-order-harmonic spectra with  $\phi = 0^\circ, 30^\circ, 60^\circ$ , and  $90^\circ$ . The dashed purple curve indicates the cutoff regions. (b) The solid blue curve shows the CEP dependence of the cutoff energy  $\eta_{\text{cutoff}}$ . The dashed green curve shows  $|A(t)|_{\text{max}}$ . (c)  $\eta_{\text{cutoff}}$  as a function of  $|A(t)|_{\text{max}}$ . Here  $\phi$  is chosen from  $0^\circ$  to  $90^\circ$ .

Figure 6(c) shows  $\eta_{\text{cutoff}}$  as a function of  $|A(t)|_{\text{max}}$ , where  $\phi$  is chosen from the range of  $0^\circ$ – $90^\circ$ . The result confirms that  $\eta_{\text{cutoff}}$  increases linearly with  $|A(t)|_{\text{max}}$ . For a long pulse, since the CEP only slightly influences the waveform of the vector potential, the equation  $|A(t)|_{\text{max}} = A_0$  holds for any value of  $\phi$ , where  $A_0$  is the amplitude of the vector potential. Thus, the cutoff energy for long pulses satisfies  $\eta_{\text{cutoff}} \propto A_0$ , as discussed in Refs. [24,25,31,41].

In the following, we choose the cases with  $\phi = 0^\circ$  and  $\phi = 90^\circ$  as examples to analyze the CEP effect using TDPI pictures. The TDPI pictures for  $\phi = 0^\circ$  and  $\phi = 90^\circ$  are shown in Figs. 7(a) and 7(c), respectively. The corresponding  $\mathcal{E}_{C1-V}(t)$  and  $|A(t)|$  for  $\phi = 0^\circ$  and  $\phi = 90^\circ$  are shown in Figs. 7(b) and 7(d), respectively. From Figs. 7(a)–7(d), one can see that the population oscillations for  $\phi = 0^\circ$  and  $\phi = 90^\circ$  are significantly different, but both of them are determined by the respective  $|A(t)|$ . Specifically, as shown in Fig. 7(a), the population oscillation in CB1 exhibits two peaks with equal

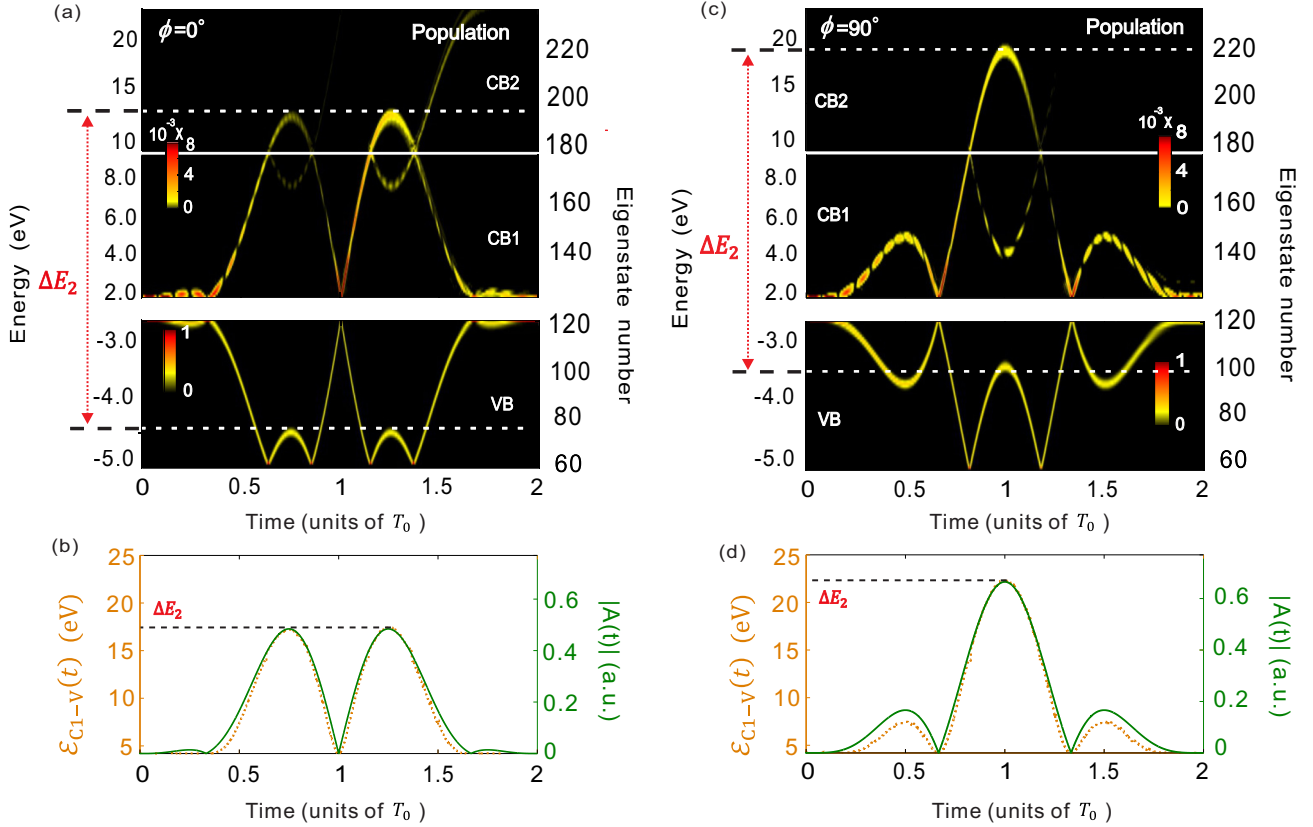


FIG. 7. (a) The TDPI picture obtained with  $\phi = 0^\circ$ . (b) The real-time radiation energy  $\mathcal{E}_{\text{C1-V}}(t)$  and  $|A(t)|$  for  $\phi = 0^\circ$ . (c) The TDPI picture obtained with  $\phi = 90^\circ$ . (d) The real-time radiation energies  $\mathcal{E}_{\text{C1-V}}(t)$  and  $|A(t)|$  for  $\phi = 90^\circ$ . In (b) and (d), the dotted yellow curves represent  $\mathcal{E}_{\text{C1-V}}(t)$ , and the solid green curves represent  $|A(t)|$ .

height. This trend is similar to that of the corresponding  $|A(t)|$  curve shown in Fig. 7(b). Likewise, as shown in Fig. 7(c), the population oscillation in CB1 exhibits a prominent peak in the middle and two secondary peaks on both sides, which is similar to the trend of the  $|A(t)|$  curve shown in Fig. 7(d). The correspondence between electronic oscillation and  $|A(t)|$  essentially originates from the fact that the wave vector of Bloch electrons depends linearly on the vector potential of the external laser field [41].

Moreover,  $|A(t)|$  not only dominates the population oscillations of electrons in their respective bands but also governs the energy differences between conduction and valence bands, i.e., the real-time photon energies of emitted harmonics. As shown in Figs. 7(b) and 7(d), one can see that  $\mathcal{E}_{\text{C1-V}}(t)$  has the same trend as  $|A(t)|$  for both  $\phi = 0^\circ$  and  $\phi = 90^\circ$ . Especially for the high-energy region,  $\mathcal{E}_{\text{C1-V}}(t)$  and  $|A(t)|$  nearly coincide completely with each other. Considering that different linear vertical axes are used for the two curves, for the high-energy region, it can be found that

$$\mathcal{E}_{\text{C1-V}}(t) \propto |A(t)|. \quad (13)$$

Equation (13) is not only valid for the short pulse used here; it has been verified by our numerous other simulations. According to Eq. (13), Eq. (12) can be obtained considering that  $\eta_{\text{cutoff}} = \max[\mathcal{E}_{\text{C1-V}}(t)]$ . Since  $|A(t)|_{\text{max}}$  for  $\phi = 90^\circ$  is larger than that for  $\phi = 0^\circ$ , as shown in Figs. 7(b) and 7(d), the cutoff energy for  $\phi = 90^\circ$  is larger than that for  $\phi = 0^\circ$ .

Based on the above discussions, the origin of the CEP effect on the cutoff energy for solid HHG can be understood as follows. When the CEP varies, the corresponding variation of  $A(t)$  leads to the changes in the Bloch oscillation in each

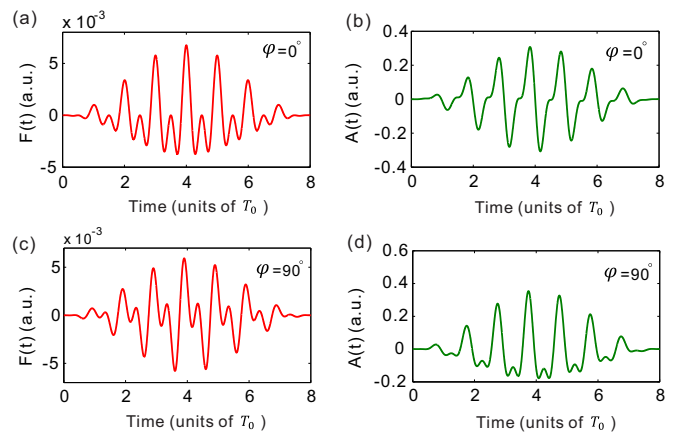


FIG. 8. The synthesized electric fields and vector potentials of the two-color laser pulse with (a) and (b)  $\phi = 0^\circ$  and (c) and (d)  $\phi = 90^\circ$ . The laser wavelengths of the fundamental and second-harmonic fields are  $\lambda_1 = 3.20 \mu\text{m}$  and  $\lambda_2 = 1.60 \mu\text{m}$ , respectively. The laser intensities of the fundamental and second-harmonic fields are both  $I = 4.00 \times 10^{11} \text{ W/cm}^2$ . The total duration of the laser pulse is eight optical cycles.

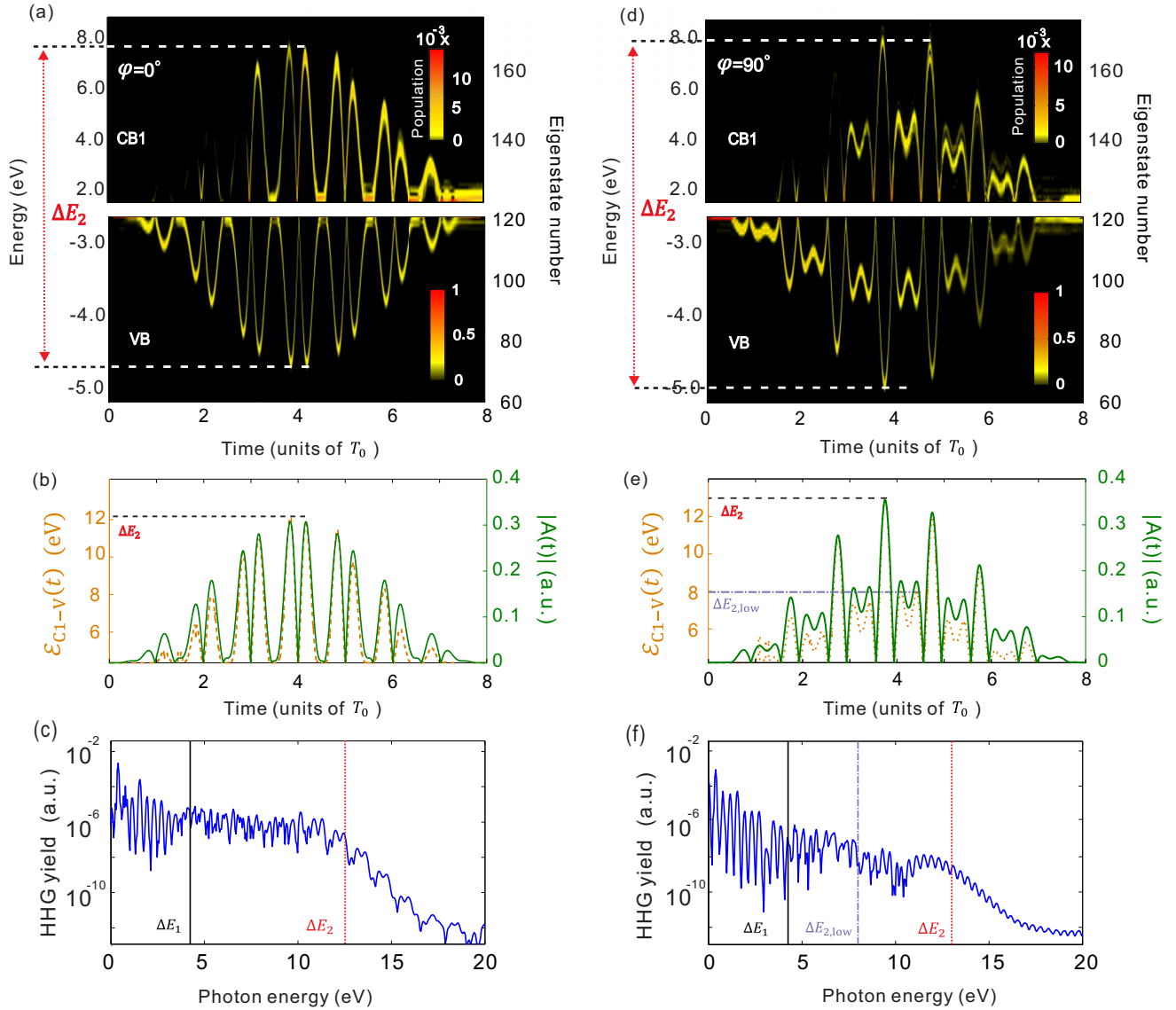


FIG. 9. (a) and (d) The TDPI picture obtained with  $\varphi = 0^\circ$  and  $90^\circ$ , respectively. (b) and (e) Comparisons between  $\mathcal{E}_{C1-v}(t)$  and  $|A(t)|$  for  $\varphi = 0^\circ$  and  $90^\circ$ , respectively. The dotted yellow curves represent  $\mathcal{E}_{C1-v}(t)$ , and the solid green curves represent  $|A(t)|$ . (c) and (f) Harmonic spectra obtained with  $\varphi = 0^\circ$  and  $90^\circ$ , respectively.

band. As a result, the maximum energy difference of oscillating electrons between the conduction band and valence band varies correspondingly, which gives rise to the change in the cutoff energy. Specifically, the cutoff energy  $\eta_{\text{cutoff}}$  is proportional to  $|A(t)|_{\text{max}}$ .

## VI. TWO-COLOR LASER FIELDS

For the gas HHG, a lot of works have been devoted to the study of HHG in two-color laser fields [55–57] because the two-color field offers a powerful tool to regulate the HHG. For instance, the two-color field can be used to amplify the HHG yield and extend the harmonic cutoff [58–60]. By varying the relative phase between the two components, the two-color field allows one to manipulate the HHG processes [61,62] and control the birth of attosecond XUV pulses [63]. The dynamical processes of HHG in the two-color field are more complicated than those in the monochromatic field. To our

knowledge, HHG driven by two-color fields in solids is rarely investigated at present.

Herein, we demonstrate the HHG dynamics in solids driven by two-color fields involving a fundamental and a second-harmonic field using TDPI pictures. In our calculation, the wavelengths of the fundamental and second-harmonic fields are  $\lambda_1 = 3.20 \mu\text{m}$  and  $\lambda_2 = 1.60 \mu\text{m}$ , respectively. The laser intensities of the two components are both  $I = 4.00 \times 10^{11} \text{ W/cm}^2$ . The total duration of the laser pulse is eight optical cycles of the fundamental field. The relative phase between the two components is denoted as  $\varphi$ . We will focus on the cases where  $\varphi = 0^\circ$  and  $\varphi = 90^\circ$  to analyze the HHG processes. The synthesized electric fields and vector potentials with  $\varphi = 0^\circ$  and  $\varphi = 90^\circ$  are shown in Figs. 8(a)–8(d).

Figures 9(a) and 9(b) show the TDPI picture and the comparison between  $\mathcal{E}_{C1-v}(t)$  and  $|A(t)|$  for  $\varphi = 0^\circ$ , respectively. The corresponding figures for  $\varphi = 90^\circ$  are shown in Figs. 9(d) and 9(e), respectively. One can see that the

population oscillations of electrons in the respective bands are still clear. According to the discussion in Sec. V, the photon energy of an emitted harmonic for the high-energy region depends linearly on  $|A(t)|$ . Hence, as shown in Figs. 9(b) and 9(e),  $\mathcal{E}_{C1-v}(t)$  curves are in good agreement with the corresponding  $|A(t)|$  curves for both  $\varphi = 0^\circ$  and  $\varphi = 90^\circ$ , respectively. Compared with the population oscillations from the monochromatic field shown in Fig. 2(a), the population oscillations shown in Figs. 9(a) and 9(d) are peculiar. The special profiles of population oscillations are determined by the corresponding  $|A(t)|$ , as shown in Figs. 9(b) and 9(e).

The high-order-harmonic spectra for  $\varphi = 0^\circ$  and  $\varphi = 90^\circ$  are shown in Figs. 9(c) and 9(f), respectively. It is shown that the starts and cutoffs of the harmonic plateaus are still very well in accord with  $\Delta E_1$  and  $\Delta E_2$  for both  $\varphi = 0^\circ$  and  $\varphi = 90^\circ$ . The cutoff energy for  $\varphi = 90^\circ$  is larger than that for  $\varphi = 0^\circ$  because  $\Delta E_2$  for  $\varphi = 90^\circ$  is greater than that for  $\varphi = 0^\circ$ , as shown in Figs. 9(a) and 9(d). This sensitivity of the cutoff energy to relative phase  $\varphi$  is essentially due to the fact that  $|A(t)|_{\max}$  changes correspondingly when  $\varphi$  varies.

In addition, the harmonic plateau for  $\varphi = 0^\circ$  shown in Fig. 9(c) is quite flat. This is because the profile of the population oscillation in the TDPI picture is composed of regular peaks similar to those for a monochromatic field. By contrast, the harmonic plateau for  $\varphi = 90^\circ$  shown in Fig. 9(f) is relatively uneven. This uneven plateau is caused by the special structure of the profile of the population oscillation in the TDPI picture and can be interpreted with the  $\mathcal{E}_{C1-v}(t)$  curve. As shown in Fig. 9(e), the  $\mathcal{E}_{C1-v}(t)$  curve is composed of two kinds of peaks: the high, sharp peaks and the low peaks with concave tops. Then, the  $\mathcal{E}_{C1-v}(t)$  curve can be divided into two parts by the maximum energy of the low peaks  $\Delta E_{2,\text{low}}$ , as indicated by the dot-dashed purple line in Fig. 9(e). The high-order harmonics with photon energy larger than  $\Delta E_{2,\text{low}}$  are emitted, at most, twice per cycle, whereas the high-order harmonics with photon energy smaller than  $\Delta E_{2,\text{low}}$  can be emitted four times per cycle. Therefore, HHG in the region below  $\Delta E_{2,\text{low}}$  is more efficient. In Fig. 9(f),  $\Delta E_{2,\text{low}}$  is

indicated by the vertical dot-dashed purple line. One can see that the intensity of the harmonics ranging from  $\Delta E_{2,\text{low}}$  to  $\Delta E_2$  is lower than that ranging from  $\Delta E_1$  to  $\Delta E_{2,\text{low}}$ .

The above results indicate that the two-color field can be used to control the electron dynamics in solids. The features of generated high-order harmonics can be modulated effectively by adjusting the relative phase of two components. The manipulation of the solid HHG with the two-color field can be guided by the TDPI picture.

## VII. CONCLUSION

In summary, this work introduced an intuitive representation called TDPI picture to reveal the electron dynamics of solid HHG in a quantitative way. The population oscillations of electrons in the respective bands were clearly demonstrated in TDPI pictures. We showed that the real-time photon energies of emitted harmonics can be obtained directly from the instantaneous energy differences of oscillating electrons. Specifically, the cutoff energies of the harmonic plateaus are determined by the maximum energy differences. In the TDPI picture, the concepts of short and long trajectories in solid HHG can be clarified clearly. By using TDPI pictures, we studied the CEP effects in short pulses and demonstrate the HHG dynamics driven by two-color fields. It was shown that the vector potential of the laser pulse dominates the dynamical processes of solid HHG. The TDPI method proposed in the present work provides a promising way to analyze the solid dynamics in a strong field, and it would be helpful to shed light on some underlying mechanisms in future studies.

## ACKNOWLEDGMENTS

The authors thank Prof. X.-B. Bian for very helpful discussions. This work was supported by the National Natural Science Foundation of China under Grants No. 11234004, No. 11404123, No. 11574101, No. 11422435, and No. 11627809.

- 
- [1] F. Krausz and M. Ivanov, *Rev. Mod. Phys.* **81**, 163 (2009).  
 [2] P. B. Corkum and F. Krausz, *Nat. Phys.* **3**, 381 (2007).  
 [3] J. Itatani, J. Levesque, D. Zeidler, H. Niikura, H. Pépin, J. C. Kieffer, P. B. Corkum, and D. M. Villeneuve, *Nature (London)* **432**, 867 (2004); C. Zhai, X. Zhu, P. Lan, F. Wang, L. He, W. Shi, Y. Li, M. Li, Q. Zhang, and P. Lu, *Phys. Rev. A* **95**, 033420 (2017); C. Zhai, L. He, P. Lan, X. Zhu, Y. Li, F. Wang, W. Shi, Q. Zhang, and P. Lu, *Sci. Rep.* **6**, 23236 (2016); M. Qin and X. Zhu, *Opt. Laser Technol.* **87**, 79 (2017).  
 [4] N. Teeny, E. Yakoboylu, H. Bauke, and C. H. Keitel, *Phys. Rev. Lett.* **116**, 063003 (2016); Y. Zhou, M. Li, Y. Li, A. Tong, Q. Li, and P. Lu, *Opt. Express* **25**, 8450 (2017); X. Ma, M. Li, Y. Zhou, and P. Lu, *Opt. Quantum Electron.* **49**, 170 (2017).  
 [5] K. Liu and I. Barth, *Phys. Rev. A* **94**, 043402 (2016); X. Zhu, P. Lan, K. Liu, Y. Li, X. Liu, Q. Zhang, I. Barth, and P. Lu, *Opt. Express* **24**, 4196 (2016).  
 [6] J. L. Krause, K. J. Schafer, and K. C. Kulander, *Phys. Rev. Lett.* **68**, 3535 (1992).  
 [7] K. J. Schafer, B. Yang, L. F. DiMauro, and K. C. Kulander, *Phys. Rev. Lett.* **70**, 1599 (1993).  
 [8] P. B. Corkum, *Phys. Rev. Lett.* **71**, 1994 (1993).  
 [9] M. Lewenstein, P. Balcou, M. Y. Ivanov, A. L'Huillier, and P. B. Corkum, *Phys. Rev. A* **49**, 2117 (1994).  
 [10] X. Zhang, X. Zhu, X. Liu, D. Wang, Q. Zhang, P. Lan, and P. Lu, *Opt. Lett.* **42**, 1027 (2017); X. Liu, P. Li, X. Zhu, P. Lan, Q. Zhang, and P. Lu, *Phys. Rev. A* **95**, 033421 (2017).  
 [11] S. Ghimire, A. D. DiChiara, E. Sistrunk, P. Agostini, L. F. DiMauro, and D. A. Reis, *Nat. Phys.* **7**, 138 (2011).  
 [12] S. Ghimire, G. Ndabashimiye, A. D. DiChiara, E. Sistrunk, M. I. Stockman, P. Agostini, L. F. DiMauro, and D. A. Reis, *J. Phys. B* **47**, 204030 (2014).  
 [13] C. Yu, X. Zhang, S. Jiang, X. Cao, G. Yuan, T. Wu, L. Bai, and R. Lu, *Phys. Rev. A* **94**, 013846 (2016).

- [14] S. Ghimire, A. D. DiChiara, E. Sistrunk, G. Ndashimiye, U. B. Szafruga, A. Mohammad, P. Agostini, L. F. DiMauro, and D. A. Reis, *Phys. Rev. A* **85**, 043836 (2012).
- [15] T. T. Luu, M. Garg, S. Y. Kruchinin, A. Moulet, M. T. Hassan, and E. Goulielmakis, *Nature (London)* **521**, 498 (2015).
- [16] A. L. Cavalieri, N. Müller, Th. Uphues, V. S. Yakovlev, A. Baltuška, B. Horvath, B. Schmidt, L. Blümel, R. Holzwarth, S. Hendel, M. Drescher, U. Kleineberg, P. M. Echenique, R. Kienberger, F. Krausz, and U. Heinzmann, *Nature (London)* **449**, 1029 (2007).
- [17] C. M. Wang, T. S. Ho, and S. I. Chu, *J. Phys. B* **49**, 225401 (2016).
- [18] G. Ndashimiye, S. Ghimire, M. Wu, D. A. Browne, K. J. Schafer, M. B. Gaarde, and D. A. Reis, *Nature (London)* **534**, 520 (2016).
- [19] G. Vampa, T. J. Hammond, N. Thiré, B. E. Schmidt, F. Légaré, C. R. McDonald, T. Brabec, D. D. Klug, and P. B. Corkum, *Phys. Rev. Lett.* **115**, 193603 (2015).
- [20] M. Schultze, K. Ramasesha, C. D. Pemmaraju, S. A. Sato, D. Whitmore, A. Gandman, J. S. Prell, L. J. Borja, D. Prendergast, K. Yabana, D. M. Neumark, and S. R. Leone, *Science* **346**, 1348 (2014).
- [21] S. Ghimire, A. D. DiChiara, E. Sistrunk, U. B. Szafruga, P. Agostini, L. F. DiMauro, and D. A. Reis, *Phys. Rev. Lett.* **107**, 167407 (2011).
- [22] B. Zaks, R. B. Liu, and M. S. Sherwin, *Nature (London)* **483**, 580 (2012).
- [23] M. Hohenleutner, F. Langer, O. Schubert, M. Knorr, U. Huttner, S. W. Koch, M. Kira, and R. Huber, *Nature (London)* **523**, 572 (2015).
- [24] M. Wu, D. A. Browne, K. J. Schafer, and M. B. Gaarde, *Phys. Rev. A* **94**, 063403 (2016).
- [25] M. Wu, S. Ghimire, D. A. Reis, K. J. Schafer, and M. B. Gaarde, *Phys. Rev. A* **91**, 043839 (2015).
- [26] T. Higuchi, M. I. Stockman, and P. Hommelhoff, *Phys. Rev. Lett.* **113**, 213901 (2014).
- [27] P. G. Hawkins, M. Y. Ivanov, and V. S. Yakovlev, *Phys. Rev. A* **91**, 013405 (2015).
- [28] A. F. Kemper, B. Moritz, J. K. Freericks, and T. P. Devereaux, *New J. Phys.* **15**, 023003 (2013).
- [29] C. R. McDonald, G. Vampa, P. B. Corkum, and T. Brabec, *Phys. Rev. A* **92**, 033845 (2015).
- [30] G. Vampa, C. R. McDonald, G. Orlando, P. B. Corkum, and T. Brabec, *Phys. Rev. B* **91**, 064302 (2015).
- [31] Z. Guan, X. X. Zhou, and X. B. Bian, *Phys. Rev. A* **93**, 033852 (2016).
- [32] G. Vampa, T. J. Hammond, N. Thiré, B. E. Schmidt, F. Légaré, C. R. McDonald, T. Brabec, and P. B. Corkum, *Nature (London)* **522**, 462 (2015).
- [33] G. Vampa, C. R. McDonald, G. Orlando, D. D. Klug, P. B. Corkum, and T. Brabec, *Phys. Rev. Lett.* **113**, 073901 (2014).
- [34] O. Schubert, M. Hohenleutner, F. Langer, B. Urbanek, C. Lange, U. Huttner, D. Golde, T. Meier, M. Kira, S. W. Koch, and R. Huber, *Nat. Photonics* **8**, 119 (2014).
- [35] P. G. Hawkins and M. Y. Ivanov, *Phys. Rev. A* **87**, 063842 (2013).
- [36] D. Golde, T. Meier, and S. W. Koch, *Phys. Rev. B* **77**, 075330 (2008).
- [37] J. C. Slater, *Phys. Rev.* **87**, 807 (1952).
- [38] B. M. Breid, D. Witthaut, and H. J. Korsch, *New J. Phys.* **8**, 110 (2006).
- [39] R. Chang, S. Potnis, R. Ramos, C. Zhuang, M. Hallaji, A. Hayat, F. Duque-Gomez, J. E. Sipe, and A. M. Steinberg, *Phys. Rev. Lett.* **112**, 170404 (2014).
- [40] T. Y. Du, Z. Guan, X. X. Zhou, and X. B. Bian, *Phys. Rev. A* **94**, 023419 (2016).
- [41] T. Y. Du and X. B. Bian, *Opt. Express* **25**, 151 (2017).
- [42] M. D. Feit, J. A. Fleck, Jr., and A. Steiger, *J. Comput. Phys.* **47**, 412 (1982).
- [43] A. Tong, Y. Zhou, and P. Lu, *Opt. Quantum Electron.* **49**, 77 (2017).
- [44] A. H. C. Neto, F. Guinea, N. M. R. Peres, K. S. Novoselov, and A. K. Geim, *Rev. Mod. Phys.* **81**, 109 (2009).
- [45] S. Ke, B. Wang, H. Long, K. Wang, and P. Lu, *Opt. Express* **25**, 11132 (2017); Q. Liu, B. Wang, S. Ke, H. Long, K. Wang, and P. Lu, *ibid.* **25**, 7203 (2017).
- [46] T. Tamaya, A. Ishikawa, T. Ogawa, and K. Tanaka, *Phys. Rev. Lett.* **116**, 016601 (2016).
- [47] C. C. Chirilă, I. Dreisigacker, E. V. van der Zwan, and M. Lein, *Phys. Rev. A* **81**, 033412 (2010).
- [48] M. Nisoli, G. Sansone, S. Stagira, S. De Silvestri, C. Vozzi, M. Pascolini, L. Poletto, P. Villoresi, and G. Tondello, *Phys. Rev. Lett.* **91**, 213905 (2003).
- [49] A. de Bohan, P. Antoine, D. B. Milošević, and B. Piraux, *Phys. Rev. Lett.* **81**, 1837 (1998).
- [50] P. Dietrich, F. Krausz, and P. B. Corkum, *Opt. Lett.* **25**, 16 (2000).
- [51] I. P. Christov, *Opt. Lett.* **24**, 1425 (1999).
- [52] Y. Li, M. Li, Y. Zhou, X. Ma, H. Xie, P. Lan, and P. Lu, *Opt. Express* **25**, 11233 (2017).
- [53] A. Baltuška, T. Udem, M. Uiberacker, M. Hentschel, E. Goulielmakis, C. Gohle, R. Holzwarth, V. S. Yakovlev, A. Scrinzi, T. W. Hänsch, and F. Krausz, *Nature (London)* **421**, 611 (2003).
- [54] J. J. Carrera and S.-I. Chu, *Phys. Rev. A* **75**, 033807 (2007).
- [55] M. V. Frolov, N. L. Manakov, A. A. Silaev, and N. V. Vvedenskii, *Phys. Rev. A* **81**, 063407 (2010); C. Yu *et al.*, *J. Phys. B* **47**, 225602 (2014).
- [56] L. Li, Z. Wang, F. Li, and H. Long, *Opt. Quantum Electron.* **49**, 73 (2017); L. Li, X. Zhu, P. Lan, L. He, and P. Lu, *arXiv:1702.04084*.
- [57] H. Yuan, L. He, F. Wang, B. Wang, W. Liu, and Z. Hong, *Opt. Quantum Electron.* **49**, 214 (2017).
- [58] S. Watanabe, K. Kondo, Y. Nabekawa, A. Sagisaka, and Y. Kobayashi, *Phys. Rev. Lett.* **73**, 2692 (1994).
- [59] T. T. Liu, T. Kanai, T. Sekikawa, and S. Watanabe, *Phys. Rev. A* **73**, 063823 (2006).
- [60] Z. Zhai and X. S. Liu, *J. Phys. B* **41**, 125602 (2008).
- [61] R. A. Ganeev, Z. Wang, P. Lan, P. Lu, M. Suzuki, and H. Kuroda, *Phys. Rev. A* **93**, 043848 (2016).
- [62] N. Ishii, A. Kosuge, T. Hayashi, T. Kanai, J. Itatani, S. Adachi, and S. Watanabe, *Opt. Express* **16**, 20876 (2008).
- [63] N. Dudovich, O. Smirnova, J. Levesque, M. Yu. Ivanov, Y. Mairesse, D. M. Villeneuve, and P. B. Corkum, *Nat. Phys.* **2**, 781 (2006).